Earth and Planetary Science Letters 471 (2017) 186–198

Contents lists available at ScienceDirect

Earth and Planetary Science Letters

www.elsevier.com/locate/epsl

Multiple stages of aqueous alteration along fractures in mudstone and sandstone strata in Gale Crater, Mars

A.S. Yen [a,*], D.W. Ming [b], D.T. Vaniman [c], R. Gellert [d], D.F. Blake [e], R.V. Morris [b], S.M. Morrison [f], T.F. Bristow [e], S.J. Chipera [i], K.S. Edgett [j], A.H. Treiman [m], B.C. Clark [h], R.T. Downs [g], J.D. Farmer [k], J.P. Grotzinger [l], E.B. Rampe [b], M.E. Schmidt [n], B. Sutter [o], L.M. Thompson [p], MSL Science Team

[a] Jet Propulsion Laboratory, California Institute of Technology, Pasadena, CA, United States
[b] NASA Johnson Space Center, Houston, TX, United States
[c] Planetary Science Institute, Tucson, AZ, United States
[d] University of Guelph, Guelph, Ontario, Canada
[e] NASA Ames Research Center, Moffett Field, CA, United States
[f] Carnegie Institution for Science, Washington DC, United States
[g] University of Arizona, Tucson, AZ, United States
[h] Space Science Institute, Boulder, CO, United States
[i] Chesapeake Energy, Oklahoma City, OK, United States
[j] Malin Space Science Systems, San Diego, CA, United States
[k] Arizona State University, Tempe, AZ, United States
[l] California Institute of Technology, Pasadena, CA, United States
[m] Lunar and Planetary Institute, Houston, TX, United States
[n] Brock University, St. Catharines, Ontario, Canada
[o] Jacobs Technology, Houston, TX, United States
[p] University of New Brunswick, Fredericton, New Brunswick, Canada

ARTICLE INFO

Article history:
Received 18 January 2017
Received in revised form 12 April 2017
Accepted 17 April 2017
Available online 16 May 2017
Editor: A. Yin

Keywords:
Mars
mineralogy
geochemistry
Curiosity rover
aqueous alteration

ABSTRACT

The Mars rover *Curiosity* in Gale crater conducted the first-ever direct chemical and mineralogical comparisons of samples that have clear parent (unaltered) and daughter (altered) relationships. The mineralogy and chemistry of samples within and adjacent to alteration halos in a sandstone formation were established by the Chemistry and Mineralogy (CheMin) X-ray diffraction (XRD) instrument and the Alpha Particle X-ray Spectrometer (APXS), respectively. The Stimson formation sandstones unconformably overlie the Murray mudstone formation and represent the youngest stratigraphic unit explored by *Curiosity* to date. Aqueous alteration of the parent sandstone resulted in a loss of half of the original crystalline mineral phases and a three-fold increase in X-ray amorphous material. Aqueous fluids extensively leached Mg, Al, Mn, Fe, Ni, Zn and other elements from the parent material, decreased the pyroxene to feldspar ratio by a factor of two, introduced Ca and mixed-cation sulfates, and both passively and actively enriched the silica content. Leaching of Mg, Al, Mn, Fe, Ni and Zn and enrichment of Si and S are also observed in alteration halos in the underlying mudstone. These observations are consistent with infiltration of subsurface fluids, initially acidic and then alkaline, propagating along fractures crosscutting the Stimson sandstone and Murray mudstone. The geochemistry and mineralogy suggest a complicated diagenetic history with multiple stages of aqueous alteration under a variety of environmental conditions (e.g. both low and moderate pH). The formation of these alteration halos post-dates lithification of the sandstones and mudstones and represents one of the youngest hydrogeologic events presently known to have occurred in Gale crater.

1. Introduction

The primary objective of the Mars Science Laboratory *Curiosity* rover is to assess the habitability of martian environments,

* Corresponding author. Address: Jet Propulsion Laboratory, Mail Stop 183-401, 4800 Oak Grove Drive, Pasadena, CA 91109, United States.
E-mail address: Albert.S.Yen@jpl.nasa.gov (A.S. Yen).

http://dx.doi.org/10.1016/j.epsl.2017.04.033

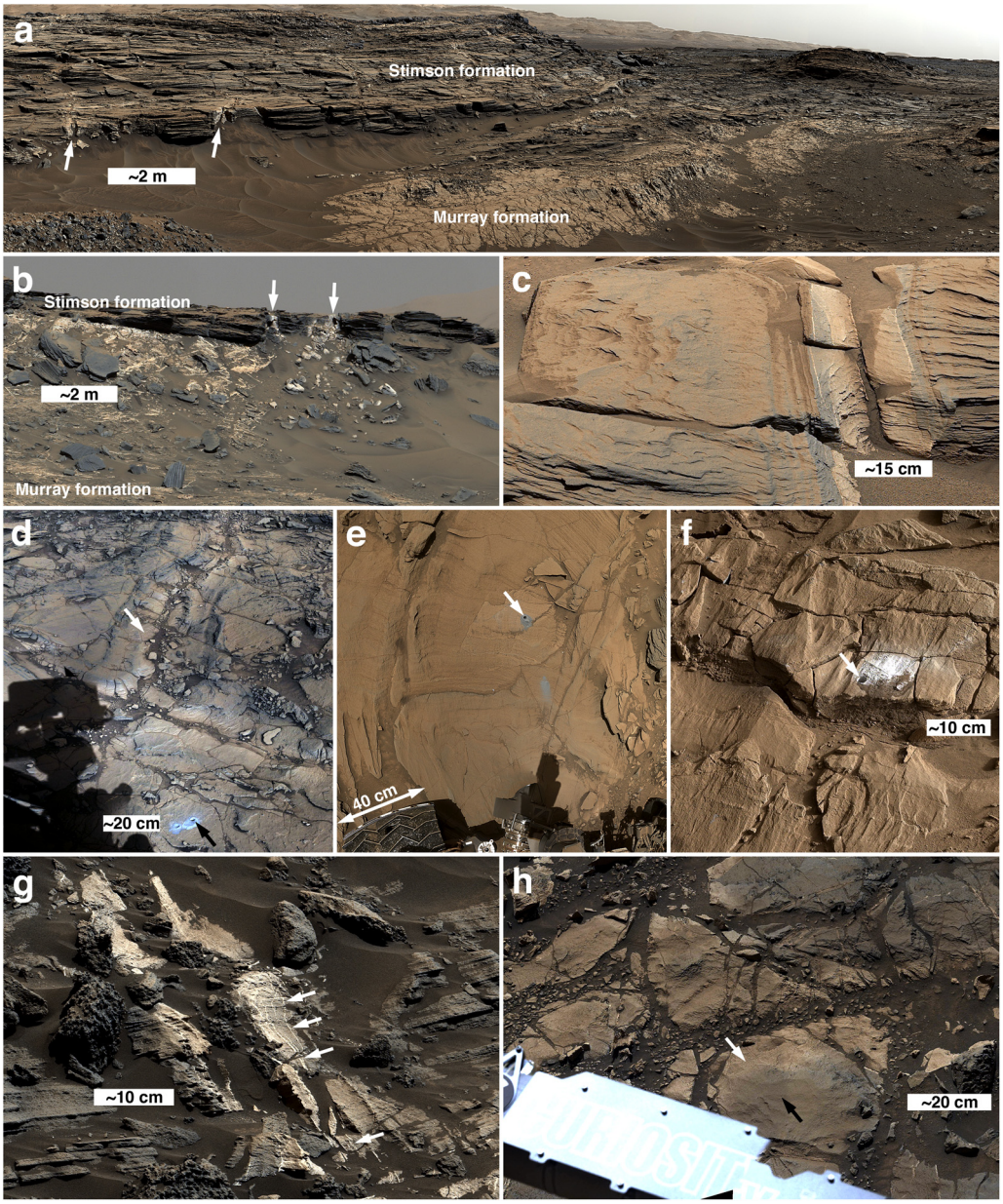

Fig. 1. (a) Murray formation mudstone overlain by Stimson formation sandstone. Fracture-associated alteration halos (arrows) are visible in the Stimson. This is a portion of Mastcam-100 mosaic mcam04395, acquired on Sol 993. (b) Alteration halos (arrows) crosscutting Stimson sandstone at the eastern edge of the Naukluft Plateau; this is a portion of Mastcam-100 mosaic mcam05931, obtained on Sol 1267. (c) Example of Stimson sandstone stratification preserved across a fracture-associated alteration halo at the Teakettle Junction outcrop; this is a portion of Mastcam-34 mosaic mcam3215, Sol 747. (d) Big Sky drill hole (parent sandstone, black arrow) and Greenhorn drill site (alteration halo, white arrow). This is a portion of a Mastcam-34 mosaic of Sol 1112, 1119, and 1126 images acquired via sequences mcam04954, mcam04956, mcam04986, and mcam05017. (e) Okoruso (parent sandstone; arrow) drill hole in a mosaic of MAHLI images acquired on Sol 1338; rover's left front wheel is seen at the lower left. (f) Lubango (alteration halo; arrow) drill hole as viewed by the Mastcam-34 shortly after drilling on Sol 1321. This is a portion of image 1321ML0063120010406076E01; note the light tone of the drill cuttings as compared to the Okoruso cuttings in (e). (g) Pervasive veins (arrows), inferred from observation of similar veins throughout the *Curiosity* field site to be calcium sulfate, in a Stimson sandstone fracture-associated alteration halo at the Mt. Shields outcrop. This is a portion of Mastcam-100 mosaic mcam04719, Sol 1073. (h) Alteration halo in Murray formation mudstone; target Cody (white arrow) is altered Murray; and target Ferdig (black arrow) is parent/unaltered Murray mudstone. This is a portion of Mastcam-34 mosaic mcam04927, Sol 1108.

both past and present. Since its August 2012 landing in Gale crater, *Curiosity* has completed over 1660 sols of surface operations, climbed 220 meters of stratigraphic section over a ~16 km traverse, collected 15 rock and multiple eolian sediment samples for detailed mineralogical and chemical analyses, and recorded the bulk compositions of hundreds of targets. *Curiosity's* instruments have provided key evidence for an ancient lacustrine environment (Grotzinger et al., 2015) with sediment sources of widely varied compositions (e.g., Treiman et al., 2016; Morris et al., 2016). *Curiosity* has found ample evidence that these sediments were affected by water, as evidenced by the replacement of olivine by clay minerals as recently as the early Hesperian epoch of martian history (Vaniman et al., 2014).

The focus here is on the silica-enriched zones that cross-cut lithified sediments and occur as ~50 cm wide, light-toned alteration "halos" surrounding central fractures (Fig. 1) in both the Murray and Stimson formations. The Murray formation mudstone is the stratigraphically lowest and oldest unit of the Mt. Sharp group sampled by *Curiosity* (Grotzinger et al., 2015). It is characterized by millimeter-scale planar laminations, moderately elevated K and Ge as well as lower Ca and Mg (Thompson et al., 2016) relative to average Mars soil (Table SI), and pervasive veining by

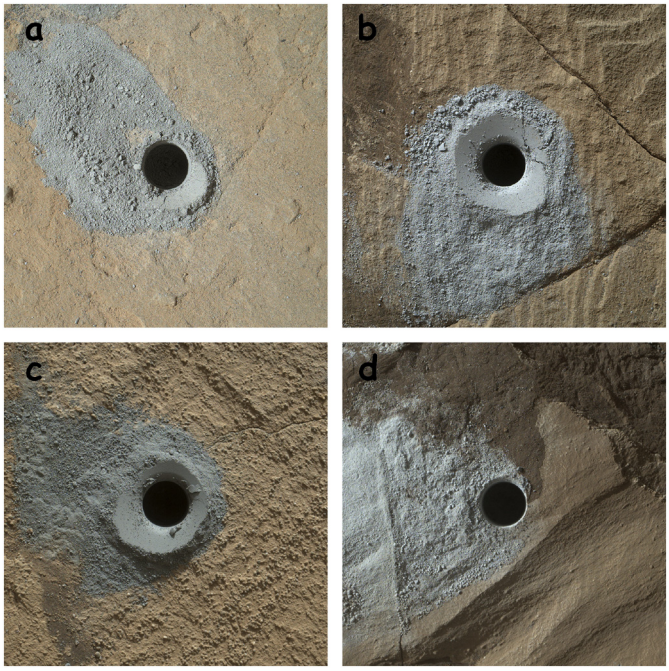

Fig. 2. MAHLI images of Stimson sandstone sample extraction drill holes; each has a diameter of 16 mm. (a) Big Sky (parent Stimson, sol 1119, 1119MH0003970010401458C00), (b) Greenhorn; note preservation of layering in the rock (alteration halo, sol 1137, image 1137MH0003970010401960C00), (c) Okoruso (parent Stimson, sol 1332, image 1332MH0005920010501230C00), (d) Lubango (alteration halo, sol 1321, image 1321MH0005920010500607C00).

millimeter- to centimeter-scale light-toned Ca-sulfates. The Stimson formation sandstone is a younger and typically cross-bedded unit chemically similar to average martian soils (Table SI). It lies unconformably over the Murray mudstone (Watkins et al., submitted for publication), and these sandstones are interpreted as lithified eolian strata (Banham et al., in preparation). The silica-enriched halos were first identified in images as light-toned bands, and their chemical compositions were established by ChemCam Laser Induced Breakdown Spectrometer (LIBS) (Wiens et al., 2012; Frydenvang et al., in press) and by APXS (Gellert and Clark, 2015) analyses. The fracture-associated halos described in this study are distinct from the high-silica, tridymite-rich material discovered in the Buckskin sample of the Murray formation (Morris et al., 2016).

2. Samples and methods

APXS elemental analyses and CheMin mineralogical analyses (Blake et al., 2012) were obtained from samples within and adjacent to the alteration halos in the cross-bedded sandstone facies (Banham et al., in preparation) of the Stimson formation. *Curiosity*'s drilled samples are homogenized rock powders collected from approximately 2 to 5 cm below the target rock surface (Anderson et al., 2012). Two such pairs of samples were acquired (Fig. 2): The first is from Greenhorn (GH, drilled on sol 1137), a light-toned fracture-associated halo sample, and Big Sky (BS, drilled on sol 1119) from the parent sandstone ~2 m lateral distance from Greenhorn (Figs. 1 and 2). The second pair of samples is from a different fracture zone ~650 m southwest of the first (Fig. 3) and includes Lubango (LB, drilled on sol 1320) in a light-toned halo and Okoruso (OK, drilled on sol 1332) from the parent sandstone ~3 m lateral distance from Lubango (Figs. 1 and 2). Supporting images were collected by *Curiosity*'s Mars Hand Lens Imager (MAHLI; Edgett et al., 2012) and mast cameras (Mastcams; Malin et al., submitted for publication).

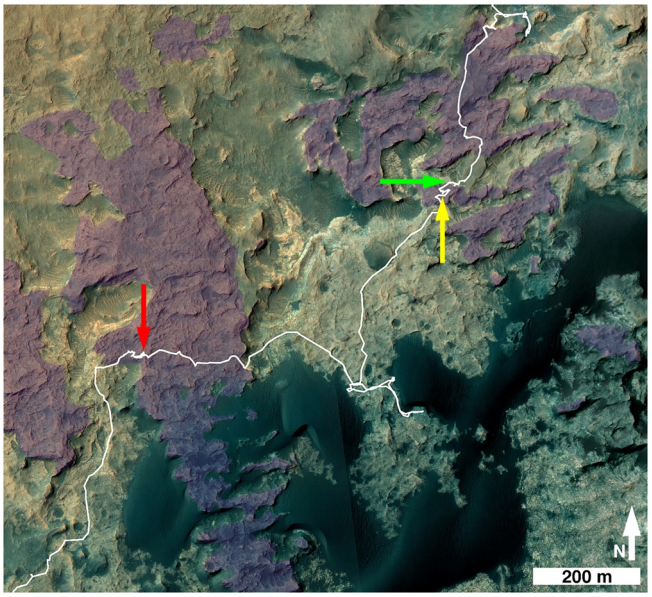

Fig. 3. Locations of the Big Sky/Greenhorn (yellow) and Okoruso/Lubango (red) drill sites in the Stimson formation sandstone. Purple shading represents Stimson formation sandstone. The green arrow indicates the location of targets Cody and Ferdig, altered and unaltered Murray formation mudstone examples (not drilled). The white line indicates the *Curiosity* rover traverse from Sol 971 (30 April 2015, upper right) through Sol 1410 (25 July 2016, lower left). The base map product, centered at 4.68°S, 137.36°E, was compiled from Mars Reconnaissance Orbiter (MRO) High Resolution Imaging Experiment (HiRISE) by Calef and Parker (2016).

2.1. Alpha Particle X-ray Spectrometer (APXS)

The arm-mounted APXS instrument determines an average chemical composition over its 1.7 cm diameter field of view by bombarding the target with alpha particles and X-rays and detecting the return of characteristic X-rays (Gellert and Clark, 2015). For each drilled sample, chemical measurements of the pre-drilled rock, the drill cuttings, and the collected fines are typically acquired. The collected fines include "pre-sieve" material (sample that has not been passed through a 150 µm sieve) and "post-sieve" material (finest size fraction of the sample; grains that passed the sieve). Including the four drill targets, the APXS has analyzed approximately 65 samples of Stimson sandstone, ~20 of which are classified as "silica-enriched" (altered). The Dust Removal Tool (DRT; Anderson et al., 2012), an actuated wire brush, has been applied to a subset of the rock targets prior to collecting APXS data. APXS chemical compositions relevant to this study are listed in Table SI.

2.2. Chemistry and Mineralogy (CheMin) instrument

The CheMin instrument is an X-ray diffractometer designed to determine the identities and proportions of crystalline mineral phases in acquired samples (Blake et al., 2012). X-rays are passed through sample cells containing post-sieved aliquots of the sample fines (<150 µm in size) and diffracted X-rays are captured by the detector. The same type of sample cells (mylar) were used for all four Stimson sandstone samples and 22.5 to 37.5 hours of integration time were accumulated for each of the samples over multiple nights of analysis. Data were processed following previously described techniques (e.g, Treiman et al., 2016) with the new addition of an empirically determined clamping offset parameter to account for differences in the distance between the sample and the detector (Morrison et al., submitted for publication). Mineralogical compositions and refined unit cell parameters for the major phases derived from fits to the diffraction patterns (Fig. 4) are listed in Table 1.

Table 1a
Crystalline mineralogy of drill samples.

	Big Sky-RAW	Big Sky-ADJ	Okoruso	Greenhorn	Lubango
Plagioclase	45.7 ± 2.2	45.6 ± 2.2	41.9 ± 2.6	42.1 ± 2.4	43.2 ± 2.4
K-feldspar	1.7 ± 0.8	1.4 ± 0.8	2.9 ± 1.0	–	–
Pigeonite	20.2 ± 1.8	21.2 ± 1.8	20.8 ± 2.0	4.7 ± 1.4	5.9 ± 1.4
Orthopyroxene	10.0 ± 2.2	10.5 ± 2.2	11.0 ± 2.2	7.6 ± 2.0	10.4 ± 2.1
Magnetite	12.6 ± 0.8	12.9 ± 0.8	17.3 ± 1.0	17.3 ± 1.0	11.1 ± 0.9
Hematite	3.6 ± 0.6	3.8 ± 0.6	1.1 ± 0.6	6.0 ± 0.8	2.3 ± 0.6
Quartz	1.6 ± 0.4	1.7 ± 0.4	1.4 ± 0.4	2.2 ± 0.6	3.5 ± 0.7
Tridymite	1.8 ± 0.4	–	–	–	–
Anhydrite	1.5 ± 0.4	1.5 ± 0.4	0.8 ± 0.6	16.1 ± 1.0	12.3 ± 0.9
Bassanite	–	–	1.2 ± 0.6	4.0 ± 1.0	9.0 ± 1.0
Gypsum	–	–	–	–	2.3 ± 0.7
Fluorapatite	1.4 ± 0.6	1.4 ± 0.6	1.6 ± 0.6	–	–
Total crystalline:	100	100	100	100	100
% Amorphous	20%	20%	35%	65%	73%

Values presented in weight percent. Uncertainties are 2σ. Crystalline components sum to 100% within the uncertainties. "Big Sky-RAW" includes contamination from the previously processed sample, Buckskin (Morris et al., 2016); this contamination was mathematically removed for the "Big Sky-ADJUSTED" result. Fitting based on the following sample cell offsets (Morrison et al., submitted for publication): Big Sky (−29 μm), Greenhorn (−46 μm), Okoruso (−25 μm), Lubango (−53 μm). Amorphous fraction of Greenhorn and Lubango constrained by chemistry and FULLPAT (Chipera and Bish, 2013) fits. The minerals listed in Table 1a represent confident detections from the CheMin datasets. The threshold of detection varies with phase and intensity of overlapping peaks but is typically 1–2 wt%. A number of additional crystalline phases were scrutinized in the fitting process but not definitively identified. These phases include olivine and ilmenite for Big Sky. For Greenhorn and Lubango, jarosite, sanidine, ilmenite and a rhombohedral carbonate can, in certain cases, improve the quality of the fit. None of these phases, however, satisfies the criteria for a positive detection. The possibility of elemental sulfur in Greenhorn and Lubango was investigated in detail; any amount present is below the detection limit.

Table 1b
Bulk mineral abundances of drill samples.

	Big Sky	Okoruso	Greenhorn	Lubango
Plagioclase	36.5 ± 1.8	27.2 ± 1.7	14.7 ± 0.8	11.7 ± 0.6
K-feldspar	1.1 ± 0.6	1.9 ± 0.7	–	–
Pigeonite	17.0 ± 1.4	13.5 ± 1.3	1.6 ± 0.5	1.6 ± 0.4
Orthopyroxene	8.4 ± 1.8	7.2 ± 1.4	2.7 ± 0.7	2.8 ± 0.5
Magnetite	10.3 ± 0.6	11.2 ± 0.7	6.1 ± 0.3	3.0 ± 0.2
Hematite	3.0 ± 0.5	0.7 ± 0.4	2.1 ± 0.3	0.6 ± 0.2
Quartz	1.4 ± 0.3	0.9 ± 0.3	0.8 ± 0.2	0.9 ± 0.2
Tridymite	–	–	–	–
Anhydrite	1.2 ± 0.3	0.5 ± 0.4	5.6 ± 0.3	3.3 ± 0.2
Bassanite	–	0.8 ± 0.4	1.4 ± 0.3	2.4 ± 0.3
Gypsum	–	–	–	0.6 ± 0.2
Fluorapatite	1.1 ± 0.5	1.0 ± 0.4	–	–
Amorphous	20 ± 10	35 ± 15	65 ± 20	73 ± 20
Total (Bulk):	100	100	100	100

Errors in crystalline fits are mathematically determined and represent 1σ values. FULLPAT errors for amorphous fraction represent 2σ values. Total bulk sums to 100% within the uncertainties.

Table 1c
Refined unit cell parameters (Morrison et al., submitted for publication) for major crystalline components of parent and silica-enriched Stimson sandstone samples.

Phase	Sample	a (A)	b (A)	c (A)	α (°)	β (°)	γ (°)	V (A^3)	Chemistry
Plagioclase	BS	8.159 ± 0.008	12.875 ± 0.008	7.103 ± 0.007	93.47 ± 0.06	116.09 ± 0.04	89.97 ± 0.05	669 ± 1	An(54 ± 5)
	OK	8.160 ± 0.008	12.880 ± 0.007	7.108 ± 0.006	93.59 ± 0.07	116.17 ± 0.04	89.91 ± 0.06	669 ± 1	An(40 ± 5)
	GH	8.165 ± 0.007	12.891 ± 0.009	7.108 ± 0.007	93.24 ± 0.07	116.10 ± 0.04	90.06 ± 0.04	670 ± 1	An(44 ± 5)
	LB	8.166 ± 0.009	12.891 ± 0.009	7.111 ± 0.009	93.26 ± 0.09	116.21 ± 0.05	90.04 ± 0.04	670 ± 1	An(33 ± 7)
Orthopyroxene	BS	18.27 ± 0.02	8.99 ± 0.01	5.216 ± 0.008	90	90	90	856 ± 2	$(Mg_{0.44\pm0.07}, Fe_{1.56})Si_2O_6$
	OK	18.31 ± 0.02	8.95 ± 0.01	5.242 ± 0.008	90	90	90	859 ± 2	$(Mg_{0.44\pm0.26}, Fe_{1.56})Si_2O_6$
	GH	18.35 ± 0.02	8.96 ± 0.01	5.257 ± 0.008	90	90	90	864 ± 2	$(Mg_{0.40\pm0.12}, Fe_{1.60})Si_2O_6$
	LB	18.32 ± 0.02	8.96 ± 0.01	5.249 ± 0.008	90	90	90	861 ± 2	$(Mg_{0.36\pm0.16}, Fe_{1.64})Si_2O_6$
Pigeonite	BS	9.672 ± 0.009	8.886 ± 0.009	5.222 ± 0.009	90	108.56 ± 0.05	90	425 ± 1	$(Mg_{1.5\pm0.1}, Ca_{0.1\pm0.05}, Fe_{0.4\pm0.1})Si_2O_6$
	OK	9.667 ± 0.009	8.891 ± 0.009	5.217 ± 0.009	90	108.51 ± 0.05	90	425 ± 1	$(Mg_{1.4\pm0.1}, Ca_{0.1\pm0.05}, Fe_{0.5\pm0.1})Si_2O_6$
Magnetite	BS	8.389 ± 0.002	8.389 ± 0.002	8.389 ± 0.002	90	90	90	590.30 ± 0.06	$Fe_{2.9\pm0.1}O_4$
	OK	8.383 ± 0.002	8.383 ± 0.002	8.383 ± 0.002	90	90	90	589.20 ± 0.06	$Fe_{2.9\pm0.1}O_4$
	GH	8.387 ± 0.002	8.387 ± 0.002	8.387 ± 0.002	90	90	90	590.03 ± 0.06	$Fe_{2.9\pm0.1}O_4$
	LB	8.380 ± 0.002	8.380 ± 0.002	8.380 ± 0.002	90	90	90	588.48 ± 0.06	$Fe_{2.9\pm0.1}O_4$
Hematite	BS	5.039 ± 0.004	5.039 ± 0.004	13.85 ± 0.01	90	90	120	304.5 ± 0.3	see text
	GH	5.060 ± 0.004	5.060 ± 0.004	13.81 ± 0.01	90	90	120	306.3 ± 0.3	see text
Anhydrite	GH	7.011 ± 0.003	7.001 ± 0.003	6.232 ± 0.002	90	90	90	305.9 ± 0.3	$(Ca_{0.98}, Fe_{0.02})SO_4$
	LB	7.012 ± 0.004	6.998 ± 0.004	6.228 ± 0.002	90	90	90	305.6 ± 0.3	$CaSO_4$

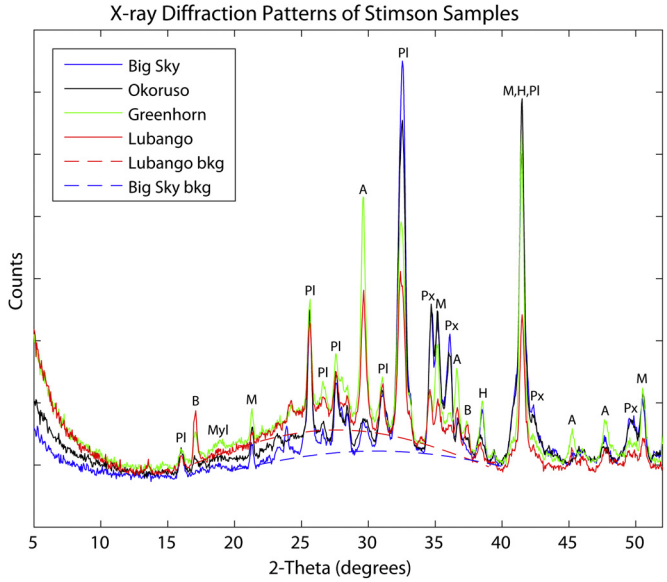

Fig. 4. X-ray diffraction patterns of silica-enriched (Greenhorn/Lubango) and parent (Big Sky/Okoruso) Stimson sandstone: A = anhydrite, B = bassanite, H = hematite, M = magnetite, Pl = plagioclase feldspar, Px = pyroxene, Myl = mylar sample cell window. The higher background in the altered samples (dashed red) represents a larger fraction of X-ray amorphous material.

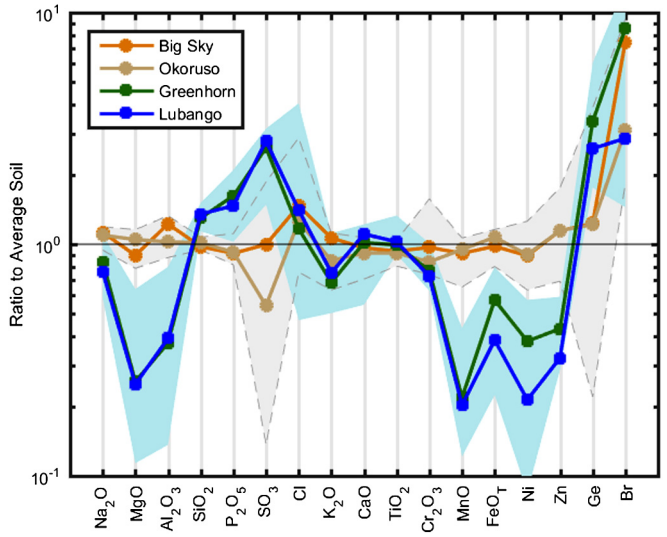

Fig. 5. Oxide ratios of silica-enriched (Greenhorn and Lubango) and parent (Big Sky and Okoruso) Stimson targets to average soil composition (Table SI). Shaded regions represent data from all APXS analyses of Big Sky, Okoruso, Greenhorn and Lubango: Pink for silica-enriched Stimson; blue for the parent sandstone. Plotted lines are averages of drill fines for each specific target. With the exception of the unusually low sulfur content of Okoruso and the typically variable bromine content of martian samples, parent Stimson has a soil-like composition. Samples from the alteration halos are enhanced in Si, P and S and depleted in Mg, Al, Mn, Fe, Ni and Zn relative to the parent material.

3. Results

3.1. Parent Stimson (Big Sky and Okoruso)

3.1.1. Elemental chemistry

Parent Stimson sandstone samples exhibit moderate variability in APXS-determined compositions. Their chemical compositions are similar to that of average martian soils (Table SI), but notable differences occur in S, Cl and Br (Fig. 5). Enrichment of these readily mobile elements on sandstone surfaces relative to martian soil is not unusual; however, the 0.65 ± 0.05 wt% SO_3 measured from the interior fines of Okoruso was unanticipated. Typical APXS measurements of parent Stimson show 3–7 wt% SO_3, and the Okoruso sample has the lowest SO_3 measured by APXS through sol 1660 at Gale crater. This low concentration of SO_3 might indicate a localized loss of soluble sulfates or a heterogeneous accumulation of sulfur (Section 3.1.4). Among the major rock forming elements in the Stimson sandstone, the greatest variability is found in FeO_T (14.8 to 25.6 wt%) and Al_2O_3 (8.2 to 12.4 wt%). Irrespective of the variability in iron, the FeO:MnO ratio remains close to 50, typical of relatively unaltered martian samples (Ming et al., 2008). MgO and SiO_2 vary by a few weight percent (absolute) in the parent Stimson sandstone targets analyzed by the APXS.

3.1.2. Crystalline constituents

The crystalline mineral phases detected in Big Sky and in Okoruso, the parent sandstones, are listed in Table 1. The presence of 1.4% tridymite in Big Sky-RAW (Table 1a) is attributed to a 10% contamination from the immediately preceding sample, Buckskin, which contained 13.6 wt% tridymite (Morris et al., 2016). An adjustment was made for this cross-contamination from the drilling, sieving and portioning hardware by subtracting from Big Sky-RAW 10% of the bulk mineral proportions of the Buckskin sample and renormalizing. The Big Sky-ADJ values in Table 1a represent the best estimate of the mineralogical composition of this sample.

Big Sky and Okoruso are similar and are dominated by plagioclase feldspar and pyroxenes (Table 1), consistent with a basaltic sediment source for these parent sandstones. The feldspar to pyroxene ratios (1.4 to 1.5) are identical within analytical uncertainties. Both samples contain abundant magnetite. However, the concentration in Okoruso is distinctly higher, 17.3 versus 12.9 wt% in the crystalline fraction, even though FeO_T differs by less than 1 wt% between the post-sieve fines of Big Sky (21.5 wt%) and Okoruso (22.4 wt%) (Table SI). Hematite represents a larger fraction of the total crystalline iron oxides in Big Sky in comparison to Okoruso, and the large unit cell volumes 304.5 $Å^3$ (Big Sky) and 306.3 $Å^3$ (Okoruso) (Table 1c) relative to ~301.7 $Å^3$ for an ideal Fe_2O_3 is suggestive of a fine-grained form (Schroeer, 1970). Bassanite, a hydrated calcium sulfate, is observed in the Okoruso sample but not detected in Big Sky. Both samples, however, contain minor anhydrite.

Olivine or fluorapatite may be present in the parent Stimson samples at or near their detection limits (1 to 2 wt%). Fluorapatite is reported in Table 1, but olivine could also be responsible for the diffraction intensity attributed to fluorapatite. In contrast, active and recently active eolian sands at Gale crater, the Bagnold Dune (Achilles et al., submitted for publication) and Rocknest sand shadow (Blake et al., 2013; Bish et al., 2013), which are chemically similar to the parent Stimson, contain 15 to 20% by weight olivine and no detectable fluorapatite. The striking difference in olivine content between these modern eolian deposits and the parent Stimson samples could indicate that the basaltic precursors are unrelated, that olivine was lost in the source region, or that the material found in the Stimson samples originally contained olivine that was altered during diagenesis (e.g., Vaniman et al., 2014) prior to formation of the alteration halos. The roughly 10–11 wt% magnetite in the bulk sample, which is a strong candidate for a cementing agent in the sandstone, could be a product of oxidative diagenesis of such pre-existing olivine. The magnetite unit cell dimensions obtained by Rietveld refinement (Table 1c) indicate a cell size slightly smaller than stoichiometric magnetite (Fe_3O_4, $a = 8.394$ Å), indicative of cell vacancies or substitutions of smaller cations (Morrison et al., submitted for publication). Unfortunately, this result does not uniquely constrain the magnetite as detrital or diagenetic; both options remain as possibilities.

3.1.3. Amorphous material

Another candidate for the cement in the Stimson sandstone is an amorphous component that has insufficient atomic order to produce sharply defined diffraction peaks. Its presence in the samples is recognized by a broad background "hump" in the diffraction pattern (Fig. 4). The shape and center of this hump depends on chemical composition: As the silica content of the amorphous component increases, the background hump becomes narrower and its centroid shifts to lower 2-theta values. The FULLPAT fitting algorithm (Chipera and Bish, 2013) uses this information to estimate the likely composition and abundance of the amorphous material. Results from FULLPAT show that both parent Stimson samples contain a significant fraction of amorphous material (20% in Big Sky; 35% in Okoruso), with compositions consistent with silica-rich glasses. However, the relative peak locations suggest a higher silica content in the Okoruso amorphous material which is best modeled with the silica content of a rhyolitic glass. The Big Sky amorphous peak is centered at a larger 2-theta value, and is best represented by a lower silica content.

The combination of CheMin crystalline mineralogy, APXS bulk chemical composition and a FULLPAT determination of the proportions of crystalline and X-ray amorphous materials enables calculations of the composition of the non-crystalline portion of each sample. These mass balance calculations involve subtraction of chemical contributions by crystalline components from the bulk APXS composition. The amorphous materials in the parent Stimson samples, Big Sky and Okoruso, are dominated by SiO_2 (Fig. 6), with variable but significant proportions of MgO, FeO_T, CaO and Al_2O_3. The higher silica content of the Okoruso amorphous material relative to Big Sky inferred by the shape and location of the background peak is supported by this calculation (Fig. 6). SO_3 is the second most abundant constituent in the X-ray amorphous component of the Big Sky sample, but is nearly absent in Okoruso, possibly indicative of a loss of soluble amorphous sulfates (the percentage of crystalline sulfates in Big Sky and Okoruso are comparable).

3.1.4. Alteration history of parent Stimson

The sand grains of the parent Stimson sandstone were likely homogenized by eolian transport prior to its lithification (Banham et al., in preparation), and sampling of the Big Sky and Okoruso targets was intended to capture unaltered material. The following lines of evidence, however, suggest that Big Sky may be more representative of the original sandstone than Okoruso. In addition to the higher silica content implied by the amorphous peak location and by calculations of the amorphous phase chemistry, the Okoruso sample also contains a hydrated calcium sulfate, bassanite, which is absent above the detection limit in Big Sky. The refinement of unit cell parameters suggests that the plagioclase feldspar in Okoruso is less calcic in comparison to the plagioclase in Big Sky (Table 1c), consistent with a loss due to weathering. The values of FeO/MnO (Table SI) are larger for Okoruso in comparison to those for Big Sky, suggesting alteration of the Okoruso sandstone sample. Finally, the unusually low SO_3 content of the Okoruso drill cuttings may also be an indicator of post-depositional alteration.

3.2. Stimson alteration halos (Greenhorn and Lubango)

3.2.1. Elemental chemistry

APXS analyses of the alteration halos in the Stimson sandstone show that they are characterized by elevated SiO_2 concentrations (50 to 67 wt%) that generally vary inversely with measured levels of FeO_T (15 to 4 wt%). Ni, Zn and MnO correlate well with FeO, and the average FeO:MnO ratio (~100) is roughly double that of typical, unaltered martian samples. The light-toned Stimson samples have among the highest concentrations of SO_3 (>15 wt%)

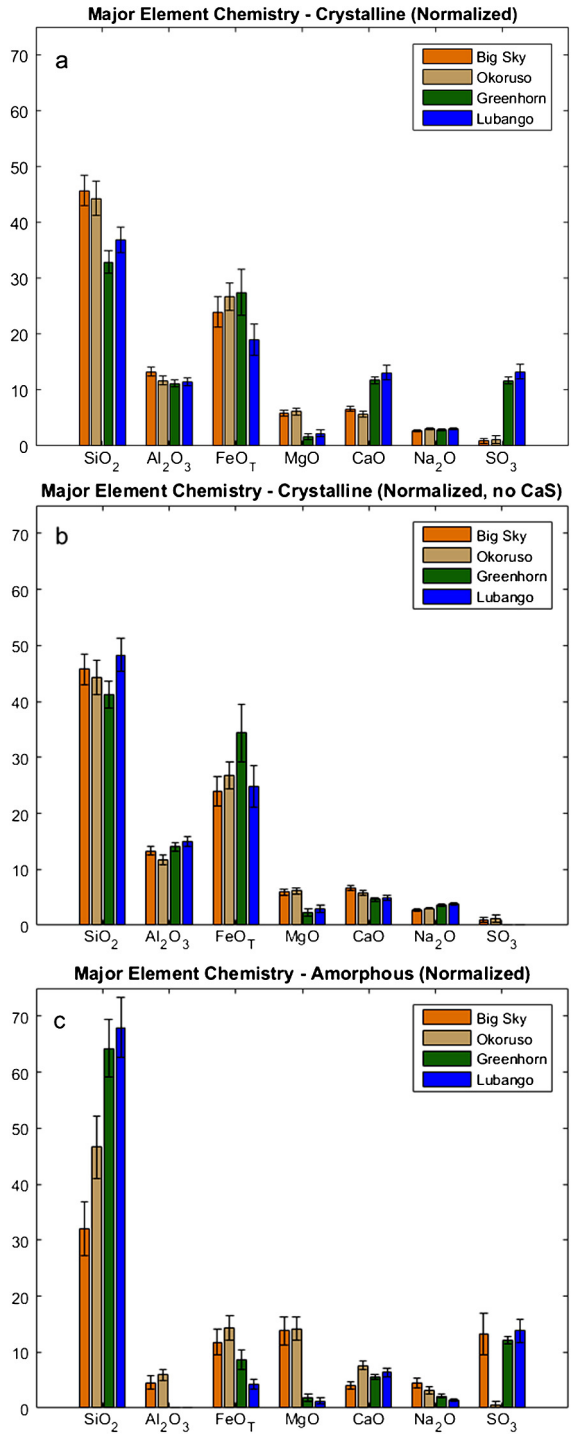

Fig. 6. Normalized chemical compositions of the crystalline (a) and amorphous (c) components of the samples (values from Table SII). The chemistry of the amorphous component is dominated by silica and has zero Al_2O_3 and very little MgO. (b) Removal of the Ca-sulfate from the crystalline fraction of the silica-enriched Greenhorn and Lubango targets results in a chemistry similar to the parent Big Sky and Okoruso samples, except for higher Fe in Greenhorn and lower Mg in both silica-enriched samples.

observed at Gale crater, not including direct analyses of Ca-rich sulfate veins. Ca correlates with SO_3 in silica-enriched Stimson samples but there is far more SO_3 than Ca, and thus, Ca cannot be the only cation for the sulfur. P_2O_5 and TiO_2 correlate weakly with SiO_2, and several samples of silica-enriched Stimson have significantly depleted MgO and/or Al_2O_3 concentrations (below 2 wt%, Table SI).

3.2.2. Crystalline mineralogy

The crystalline mineral phases and abundances given by the CheMin data for the drilled samples from the silica-enriched Stimson are generally similar (Table 1). Plagioclase feldspar and pyroxenes represent more than half of the crystalline material in Greenhorn and Lubango with feldspar:pyroxene ratios of 3.4 and 2.7, respectively. Iron oxides, with magnetite as the dominant phase, represent 13 wt% (Lubango) to 23 wt% (Greenhorn) of the crystalline portion of the samples. The small unit cell dimensions for magnetite suggest that it may be cation-deficient, but it is not possible to tell if the magnetite is diagenetic or igneous on the basis of its cell parameters. The unit cell volume for hematite in the Greenhorn sample is larger than typical, which could imply that it is very fine-grained (Schroeer, 1970). Quartz is confidently identified in the CheMin data for the first time in the Lubango sample; previous reports of quartz (e.g., Bish et al., 2013; Treiman et al., 2016) were near detection limits. Calcium sulfates with differing hydration states represent 20 to 24 wt% of the crystalline fraction of the silica-enriched Stimson samples. Anhydrite is the most abundant, but bassanite is also present. Unit cell parameters of the anhydrite are consistent with pure $CaSO_4$, though impurities such as Fe which expand the cell volume cannot be ruled out for the anhydrite in Greenhorn. Gypsum is present in the Lubango sample, the first-ever in-situ detection of gypsum on Mars, but it was not detected in Greenhorn. Gypsum dehydrates to bassanite on the timescale of several days when exposed to the elevated temperatures within the rover (Vaniman et al., 2017), so the results which average data collected over seven sols on Mars (Table 1) could represent an underestimate for the amount of gypsum originally in Lubango. Similarly, it is possible that small amounts of gypsum (<2%) could have been present in the Greenhorn sample at the time of drilling. Even though the silica-enriched Stimson samples contained extraordinary high abundances of sulfur (13 wt% and 15 wt% SO_3 equivalent in the Greenhorn and Lubango drill cuttings, respectively), no other crystalline S-bearing phases, including elemental sulfur, were detected by CheMin.

3.2.3. Amorphous component

The Greenhorn and Lubango silica-enriched samples are dominated by X-ray amorphous material. In both samples, the amorphous humps have nearly identical shapes and peak locations, consistent with the silica content of pure opal-A or a rhyolitic glass. A FULLPAT fit provided the initial estimate of the percentage of amorphous material in each silica-enriched Stimson sample (Table 1), and these values were further constrained using the combination of mineral chemistry and bulk elemental composition. The low Al_2O_3 abundances in the alteration halos (~3 wt%) limit the amount of crystalline feldspar that can be present in the sample. The 65% and 73% amorphous proportions for Greenhorn and Lubango, respectively, correspond to zero remaining Al_2O_3 in the amorphous material (and all of the Al_2O_3 in plagioclase) and should be considered lower limits (Table SII).

The chemical compositions of the amorphous fractions of the alteration halos are remarkably similar and are dominated by SiO_2, SO_3, FeO_T and CaO (Fig. 6). Relative to an average Mars soil composition (Table SI), the Greenhorn and Lubango amorphous fractions are significantly depleted in Al_2O_3, MgO and FeO_T but enhanced in SiO_2 and SO_3. The ratio of crystalline to amorphous SiO_2 in the alteration halos is approximately 1:5, and after renormalization to 100%, the non-crystalline portions of the samples contain 64 to 68 wt% SiO_2. Most of this SiO_2 must be present as amorphous silica, consistent with the FULLPAT fits, as few other elements remain for forming other compounds (Table SII). Two-thirds to three-fourths of the SO_3 resides in the amorphous fraction. The proportions of Ca, Na, Mg and K cations in the amorphous materials, however, are not adequate to fully charge-balance the abundance of $SO_4^{(2-)}$. Thus, the occurrence of mixed-cation sulfates, including iron-bearing sulfates, is necessary. The Sample Analysis at Mars (SAM) instrument (Mahaffy et al., 2012) evolved gas analyses support these results and indicate the presence of iron and magnesium sulfates in the Greenhorn sample; these sulfates must be either crystalline and below the detection limit of CheMin or present in the amorphous material (Sutter et al., submitted for publication).

4. Comparisons of alteration halos with parent rock

The differences between silica-enriched and parent Stimson sandstone can be assessed on the basis of imaging, crystalline mineralogy, amorphous composition and elemental chemistry.

4.1. Imaging

Alteration halos are visually characterized by a lighter-toned appearance relative to the parent sandstone. MAHLI images at a scale of approximately 30 μm/pixel show that the typical sand grains, including clasts of more than 1 mm in size, are transformed from a dark grey to a nearly white tone in fracture associated halos accounting for the overall lighter tone (Fig. 7). Some of the coarser sand grains developed small pits during the alteration process, possibly due to dissolution of phenocrysts at the surface, but their general shape as well as the overall sedimentary structure (bedding) remains intact (Fig. 7 a/b). Alteration halos are sometimes bounded by thin (millimeter- to centimeter-scale) light-toned veins, consistent with calcium sulfate, with apparently little or no alteration in the parent rock beyond the vein (Fig. 7 c/d).

4.2. Mineralogy

Mineralogically, the Greenhorn and Lubango samples are distinct from the parent material represented by Big Sky and Okoruso. Compared to parent Stimson, the fracture-associated halo samples exhibit significant changes in the proportions of silicate and oxide minerals and major additions of calcium sulfates (Table 1a). In the bulk sample (Table 1b), only ~40% of the original feldspar remains after alteration, but this is not simply a result of dilution from an addition of Ca-sulfates and amorphous silica. The feldspar to pyroxene ratios for samples from the alteration halos are roughly a factor of two higher than for the parent Stimson, indicating the greater susceptibility of pyroxenes to alteration. This ratio would not change if the pre-existing minerals were simply diluted by additive phases. In addition, the unit cell refinements for plagioclase suggest a decrease in the An# from Big Sky to Greenhorn and from Okoruso to Lubango, consistent with the expectation that the calcic portions of the feldspar are more readily altered (Stefansson et al., 2001). Iron oxides remain abundant in the silica-enriched sandstone, but the amount of magnetite is roughly half that of the parent Stimson. Greenhorn and Lubango record the largest totals for crystalline calcium sulfates (>6 wt% in the bulk samples) measured to date by CheMin. In contrast, parent Stimson samples contain less than 1.5 wt% Ca-sulfate. These CheMin analyses also include the first-ever direct detection of Ca-sulfate with three different hydration states in the same sample (Lubango).

The chemical constituents of the identified crystalline mineral phases normalized to 100% (Fig. 6a) reflect the addition of Ca-sulfates to the rock within the alteration halos. Interestingly, if the crystalline Ca-sulfates are removed (Fig. 6b), the major chemical components of the silica-enriched and parent Stimson crystalline mineralogy are strikingly similar. The exceptions include an increase in Fe in Greenhorn and a loss of Mg from alteration of pyroxenes. This general similarity suggests that a portion of the parent sandstone remains intact through the alteration process and

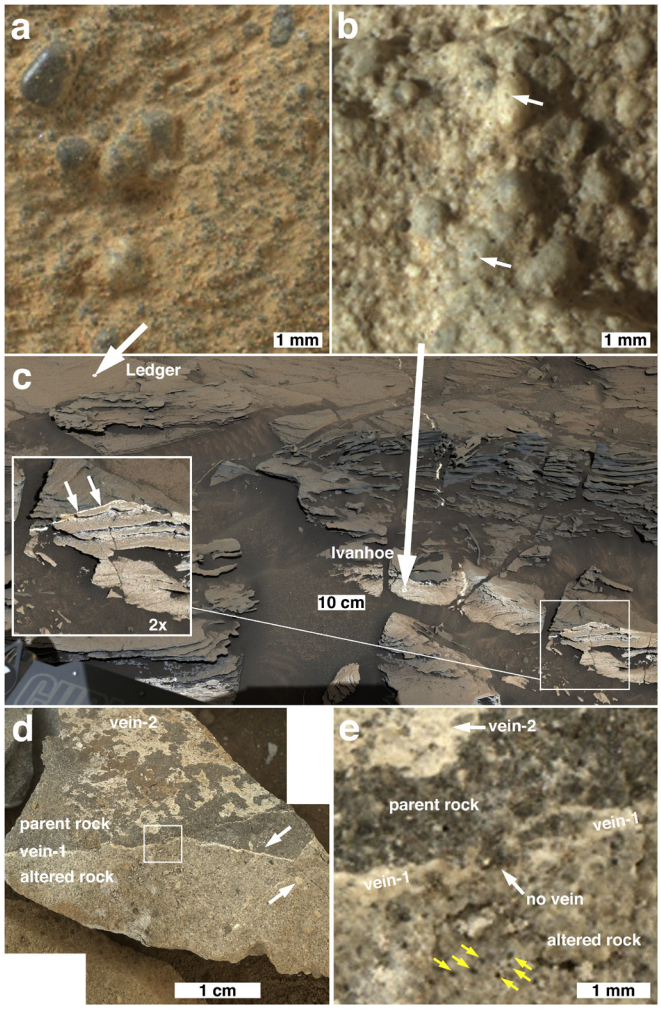

Fig. 7. (a) Unaltered parent Stimson sandstone at brushed target, Ledger, with dark grey, mm-scale, rounded sand grains; portion of MAHLI image 1092MH0002990010400991C00. (b) Shown at same scale as the Ledger example is a fracture-associated altered Stimson sandstone at target named Ivanhoe where mm-scale rounded sand grains are lighter toned in comparison to those in (a). The arrows point to examples of pits on grain surfaces which might have resulted from the alteration process(es); portion of MAHLI image 1092MH0002990010400959C00. (c) Context view of the outcrop at which Ledger and Ivanhoe occur; this is ~100 m from the Big Sky/Greenhorn drill site. The fracture associated with the alteration halos is obscured in the foreground by windblown sand. The arrows in the magnified (2×) inset indicate a light-toned vein that occurs at a sharp boundary between the altered and unaltered sandstone. The contact between altered and unaltered sandstone appears to be more diffuse where not bounded by a vein. Note that the halo alteration cuts across the original cross-bedding of the sandstone, and that the bedding structure remained intact following alteration. This is a portion of a Mastcam-34 mosaic (mcam04780) acquired on Sol 1087. (d) Rock fragment, target named Impalila, broken and displaced by *Curiosity*'s wheels from a fracture-associated halo ~1 m from the Okoruso and Lubango drill holes. The altered and parent rock surfaces exposed by breakage are indicated, as are light-toned materials from two formerly intersecting veins. Vein-1 is a fracture fill that was nearly vertical to the broken rock face; vein-2 occurs along the broken rock face, nearly perpendicular to vein-1. Relative to the parent rock, sand grains in the altered fraction retained their shape, but are light-toned, as is the matrix; parent and altered grains indicated by arrows. The white box shows the location of the higher-resolution view shown in (e). This is a mosaic of MAHLI focus merge products 1345MH0006150000501780R00 and 1345MH0006150000501782R00. (e) Detailed view of transition between altered and unaltered (or less altered) Stimson sandstone at the broken rock, Impalila. Light-toned vein-1 generally demarks the abrupt transition from darker, parent sandstone to lighter, altered sandstone; however, the white arrow indicates a sub-millimeter area where the transition is just as sharp but no vein is present (possibly an indicator that the fracturing and vein mineralization occurred after the fracture-associated halo alteration). Dark speckles (yellow arrows) may be indicators of incomplete alteration. This is a sub-frame of MAHLI focus merge product 1345MH0006150000501780R00.

that Ca-sulfate (along with other sulfur-containing phases) was added during the alteration process. Iron, as magnetite or hematite, may also have been added to the Greenhorn sample during alteration.

4.3. Amorphous phase composition

The amorphous and poorly crystalline material in the Greenhorn and Lubango alteration halo samples increased by a factor of 2 to 3 relative to the parent Stimson. In both parent and silica-enriched Stimson, the amorphous material is rich in SiO_2, but the inferred abundance of silica increases greatly in the alteration halos (Fig. 6c). The amorphous material in the parent Stimson contains ~32–47% SiO_2, compared to ~66% SiO_2 in the light-toned halos. These values correspond to 6%–16% amorphous SiO_2 in the bulk parent Stimson and 40–50% amorphous SiO_2 in the alteration halos (Table SII). Compared to the parent Stimson, the compositions of the bulk amorphous material in the silica-enriched rock show large increases in SO_3, higher proportions of CaO, decreases in MgO and a complete removal of Al_2O_3. The peak locations of the amorphous humps in the diffraction patterns also indicate that samples from the alteration halos have a higher amorphous silica content than the parent Stimson samples. The Okoruso amorphous peak is located between the peak for Big Sky and those from the silica-enriched Stimson, indicating an intermediate silica content and suggesting that Okoruso may have been partially altered.

4.4. Bulk elemental chemistry

The chemical compositions of the Greenhorn and Lubango samples are distinct from their respective parent samples (Fig. 5). Collectively, the alteration halos are characterized by substantial increases in the absolute concentrations of SiO_2 (14 wt% average increase) and SO_3 (9 wt% increase), which are balanced by losses of FeO_T (10 wt% average decrease), Al_2O_3 (7 wt% decrease) and MgO (6 wt% decrease). Several minor and trace elements not contributing significantly to the total mass exhibit large relative changes in the silica-enriched rocks: P_2O_5 (70% increase), Ge (100% increase), MnO (70% decrease), Ni (60% decrease), and Zn (60% decrease). Although FeO and MnO both decrease in the alteration zones, the FeO/MnO ratio is ~100, which is a two-fold increase from the value of ~50, typical of unaltered martian material (Ming et al., 2008). The Ge/Si ratio in the halos is nearly twice that in the parent Stimson, and the Si/Ti ratio is ~20% higher in the halos. Ni is well correlated with FeO_T, MnO, and Zn in the silica-enriched Stimson, and all of these metals trend towards zero concentration as Si increase (Fig. S1).

The true elemental losses and gains during production of the light-toned halos, however, are better represented in comparison to elements that are expected to be immobile through the alteration. In analyses of terrestrial weathering, titanium and zirconium are generally considered insoluble and immobile (Grant, 2005) and are commonly used as such reference elements. The APXS instrument uses an X-ray collimator made of Zr, which makes it challenging to use this element as a mass-balance reference. Titanium, on the other hand, is a relatively abundant element in martian samples and is well-quantified by the APXS technique. The Ti-referenced relative gains and losses for each element, X, is given by (Nesbitt, 1979):

$$\%\ \text{Change} = \left[(X_{\text{daughter}}/\text{Ti}_{\text{daughter}})/(X_{\text{parent}}/\text{Ti}_{\text{parent}}) - 1\right] \times 100.$$

This equation for can be rewritten to represent absolute gains and losses in weight percent

$$\text{Change (wt\%)} = X_{\text{daughter}} - X_{\text{parent}} * (\text{Ti}_{\text{daughter}}/\text{Ti}_{\text{parent}}).$$

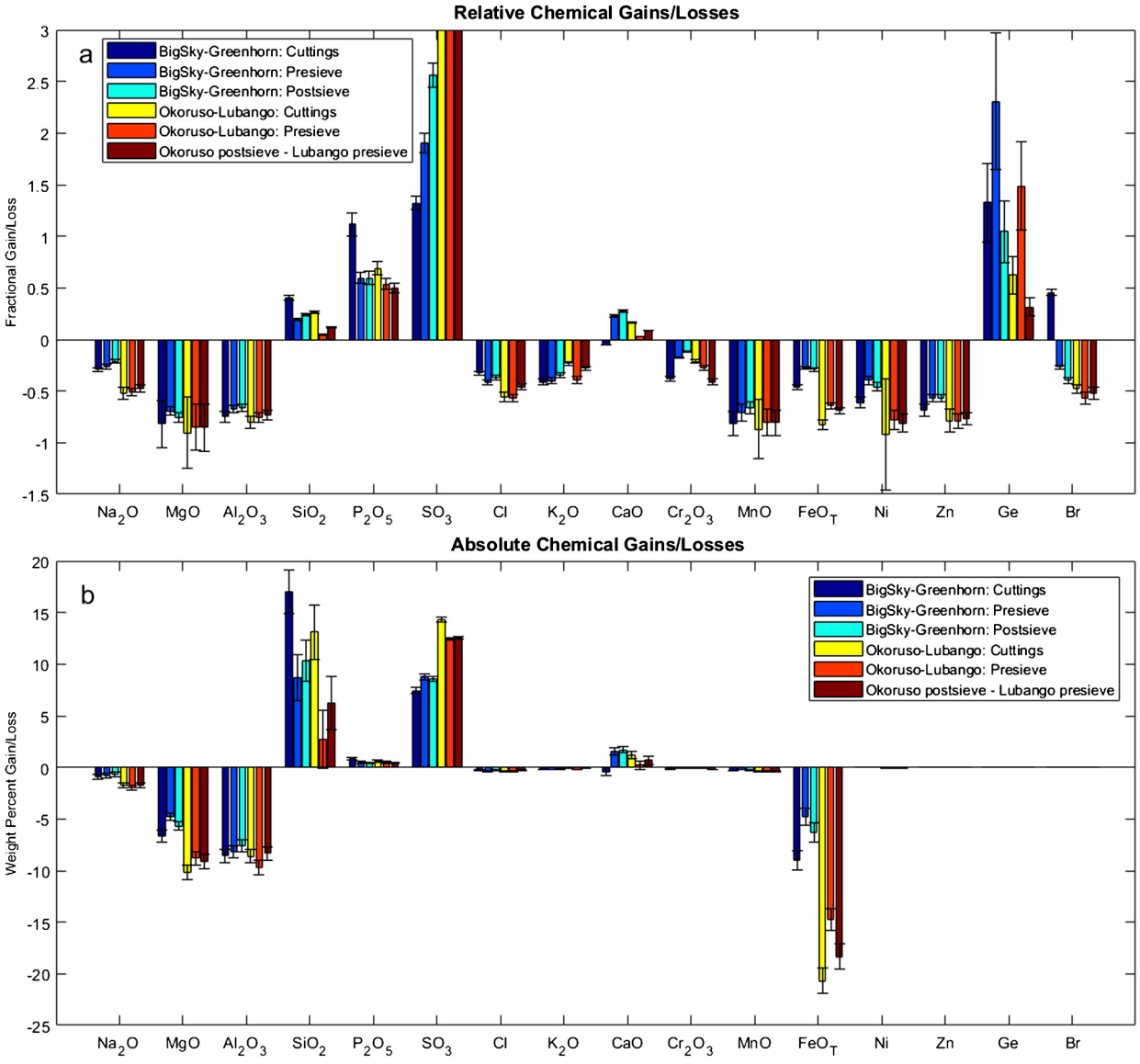

Fig. 8. Chemical gains and losses referenced to Ti, an immobile element, for corresponding samples (drill cuttings and material that did and did not pass the sieve) of parent and silica-enriched sandstone. Calculations referenced to Ti represent true losses and gains rather than changes resulting from dilution (see Section 4.4). Data are listed in Table SIII. The post-sieve measurement at the silica-enriched Lubango target was compromised, so the comparison to Okoruso (parent) uses the Lubango pre-sieve data. (a) Relative gains and losses (fraction of original concentration) referenced to Ti, (b) absolute gains and losses (weight percent) referenced to Ti.

This approach produces slightly different values (Fig. 8) compared to elemental comparisons without the Ti reference, but the fundamental results are unchanged: Significant absolute gains in SiO_2 and SO_3 balanced by losses in FeO, Al_2O_3, and MgO, as well as large relative gains in P_2O_5 and Ge and relative losses in MnO, Ni, and Zn. Na_2O, K_2O and Cr_2O_3 also exhibit significant relative losses in the alteration halos relative to the parent rock. The only major chemical component which experiences both losses and gains, depending upon which samples are compared, is CaO. Ti-referenced comparisons between Big Sky, the best representative of parent Stimson, and Lubango (rather than between Okoruso, which may be partially altered, and Lubango) also produce similar results (Table SIII).

5. Multiple alteration stages

Three general but distinct models have been proposed to explain the origin of martian samples with elevated silica concentrations: Passive silica enrichment resulting from acid-sulfate leaching of other constituents (Golden et al., 2005), direct precipitation from silica-rich fluids (Ruff et al., 2011), and the addition of detrital SiO_2-rich material (Morris et al., 2016). The third model is not applicable in this study of paired parent-daughter samples. The significant differences in water chemistry implied by the first two models are not mutually exclusive, as some terrestrial examples show large pH differences over meter-scale distances or resulting from seasonal changes in water flow (Hurwitz and Lowenstern, 2014). In fact, both passive enrichment and direct precipitation of silica are supported by the data, indicating multiple stages of fluid interaction in the formation of alteration halos in Stimson sandstone.

5.1. Acidic leaching

A crucial and inescapable factor in the formation of the light-toned halos is a major loss of aluminum, which supports the model of alteration in an acidic environment. The concentrations of Al_2O_3 in the alteration halo analyses are all less than 4 wt%, with one measurement at 1.3 wt% representing the lowest Al_2O_3 measured thus far by APXS at Gale crater. In comparison, par-

ent Stimson samples from Big Sky average approximately 10 wt% Al_2O_3. Titanium-referenced mass balance calculations (Table SIII) indicate a loss of 70% to 90% of the original aluminum. In the samples from the alteration halos, there is only sufficient aluminum for the remaining crystalline feldspar. All of the aluminum from the amorphous material as well as the aluminum from the majority of the feldspar in the parent sandstone have been completely removed from the sample. In terrestrial weathering environments, Al is mobile above pH = 11 and below pH = 4 (Oelkers et al., 1994). The major net loss of other metals (Mg, Fe, Mn, Ni and Zn) from the parent sandstone plus the likely presence of amorphous iron sulfates (discussed above) support alteration in low pH fluids with extensive leaching and removal of material. Silica is relatively immobile in comparison to these other constituents and increases in relative abundance by passive enrichment.

One significant implication of aluminum mobility is that the use of alteration indicators that rely on the stability of Al_2O_3 are invalid for these light-toned materials and for related alteration processes. The Chemical Index of Alteration (CIA) (Nesbitt and Young, 1982), for example, is based on the ratio of Al_2O_3 to ($Al_2O_3 + Na_2O + K_2O + CaO$ in silicates) and has been effectively applied in many terrestrial environments. Aluminum is assumed to be immobile, and loss of mobile Na^+, K^+ and Ca^{2+} cations increases this alteration index as feldspars transform to clay minerals. Given the clear loss of aluminum in the alteration of Stimson sandstone and other samples in Gale crater (Morris et al., 2016), however, CIA is not applicable and is not used in this study.

While acidic leaching has clearly been active in the development of the alteration halos, three aspects of the observations may initially appear inconsistent with exposure to low pH fluids. First, the presence of magnetite in the silica-enriched product is puzzling, as magnetite is readily mobilized in acidic solutions (Salmimies et al., 2011). The weathering of magnetite, however, is strongly dependent on the presence of impurities; Ti-poor magnetite is far more stable than Ti-rich magnetite and can be less susceptible to dissolution than even feldspar (Stefansson et al., 2001). The cell parameters of the magnetite identified in the alteration halos (Table 1c) are consistent with a phase containing few impurities, which may explain its stability. Second, the concentration of phosphate in the alteration halos (1.4 wt% average, Table SI) is substantially larger that of the parent Stimson (0.85 wt% average, Table SI). This is counter to what would be expected given the detection of fluorapatite in the Big Sky and Okoruso samples, as apatite is readily susceptible to acidic dissolution (Harouiya et al., 2007). If, however, the phosphorus is mobilized in acidic solution and precipitated as iron phosphate, it would remain stable in the alteration halo (McCollom and Donaldson, 2016). Finally, the preservation of parent-rock textures and grain morphology (Figs. 1c, 2b, 7) may appear to be inconsistent with extensive acidic leaching that destroys 50% of the crystalline mineralogy of the parent rock. Examples of extensive basalt leaching, however, show that pre-existing morphology (vesicles and fabric) can be clearly retained even as nearly all components except SiO_2 and TiO_2 are removed (Jakobsson et al., 2008). It is unclear whether this example is relevant to a cemented sandstone, and further work is needed to understand the retention of textures and grain morphology in the alteration halos, which may involve a yet unidentified process involving concurrent alteration and pseudomorphic replacement.

5.2. Alkaline fluids

While there is clear evidence for loss of chemical components at low pH, acidic leaching may not fully explain all compositional aspects of the alteration halos. Si:Ti ratios are generally not affected in acidic alteration (Morris et al., 2000) because neither element is particularly mobile relative to other readily-leached constituents. The Si:Ti ratios in the silica-rich halos, however, are higher than those of the parent Stimson samples, suggesting an addition of silica. Calculations of chemical gains and losses (Fig. 8) suggest ~10 wt% of the silica in Greenhorn and ~6 wt% in Lubango could have been added, perhaps liberated from underlying Murray formation rocks. The solubility and subsequent precipitation of silica is enhanced in alkaline fluids where Ti is relatively immobile, consistent with the larger Si:Ti ratio. Solubility of silica in water generally does not exceed 300 ppm unless pH values exceed 9.0 or temperatures increase above 90 °C (Krauskopf, 1956). Given that Ge concentrates in hydrothermal fluids (Bernstein, 1985), the larger Ge/Si ratios in the fracture zones could be indicators of alteration at elevated temperatures. Alternatively, the elevated Ge could simply be a signature of fluid interactions with sulfide deposits, which are typically enriched in Ge (Bernstein, 1985). The large changes in pH between acidic and alkaline conditions may reflect a natural evolution of fluid chemistry. Water-limited systems, for example, produce large changes in pH over short temporal and spatial scales (Hurwitz and Lowenstern, 2014).

Further evidence for alkaline fluid interactions in the alteration halos is the detection by the SAM evolved gas experiments of carbonate in the Greenhorn sample, but not in its Big Sky parent (Sutter et al., submitted for publication). Carbonate will not form or remain in acidic solutions, so neutral to alkaline fluid stage(s) are necessary and must post-date the acidic leaching. The amount of carbonate inferred to be present by the SAM analyses of Greenhorn is below the ~1% CheMin XRD detection limit for crystalline carbonates. The SAM instrument did not analyze the Okoruso or Lubango samples.

5.3. Calcium sulfates

The timing of the precipitation of $CaSO_4 \cdot nH_2O$ minerals in the alteration halos relative to the acidic leaching and alkaline fluid stages remains poorly constrained. On one hand, alteration halos within Gale crater are sometimes bounded by millimeter to centimeter-scale Ca-sulfate veins (Fig. 7c) suggesting that the fluids responsible for the leaching and silica enrichment came after the vein formation and could not cross this pre-existing barrier. In regions where a bounding light-toned vein are absent, the edge of the alteration halo appears more diffuse (Fig. 7c), further suggesting that the vein occurred as a pre-existing boundary. On the other hand, calcium sulfates are readily soluble over a wide range of pH (Shukla et al., 2008), and it would seem unlikely that a pre-existing vein could remain intact through an extensive acidic leaching event. It is, therefore, possible that the initial alteration produced planes of weakness or regions of higher porosity in the rock that were later infiltrated by fluids rich in Ca-sulfate.

Alternatively, the precipitation of the calcium sulfates could be roughly coeval with the acidic alteration stage. In acid mine drainage systems, for example, gypsum is one of the first phases to precipitate from the leachate (Sracek et al., 2004). Thus, if the water to rock ratio or the permeability does not favor substantial mass transport away from the acid residue, the latter stages of leaching could result in the formation of calcium sulfates without a separate fluid event. Nearly all measurements of silica-enriched alteration halos have elevated SO_3 concentrations (>10 wt%, Table SI) but no obvious Ca-sulfate veinlets. The sulfate appears homogeneously distributed in the sandstone, providing further support for acidic leaching closely followed by sulfate precipitation, as it would seem unlikely for a distinct and separate episode of Ca-sulfate fluids to coincidentally infiltrate all of the silica-enriched zones. In fact, it is rare to find Ca-sulfate veins in the Stimson which are not associated with alteration halos, and this close re-

lationship between acid sulfate alteration and gypsum veinlets is not uncommon in terrestrial volcanic settings (Zimbelman et al., 2005). Interestingly, the net difference in CaO between the alteration halo and the parent sandstone is relatively small, between −1.8 wt% and +1.7 wt% (Fig. 8), yet the bulk increase in calcium sulfate ranges from 5.3 wt% (Lubango) to 5.8 wt% (Greenhorn) (Table 1b). This indicates that the calcium in the parent rock (feldspar, pyroxenes and amorphous material) could have reprecipitated as Ca-sulfates without a significant net influx of calcium.

The coincident occurrence of gypsum, bassanite, and anhydrite is unusual. Gypsum in drilled samples readily dehydrates to bassanite ($CaSO_4 \cdot 1/2H_2O$) while held within the rover at temperatures approaching 30 °C (Vaniman et al., 2017). The transition from bassanite to anhydrite, however, occurs much more slowly and the anhydrite in the alteration halos is stable over multiple nights of analyses and is not a product of rover-related heating. Given that gypsum is modeled to be stable at the martian surface in the absence of elevated temperatures (Robertson and Bish, 2013), the origin of the abundant anhydrite in the alteration halos is unlikely to be a result of gypsum dehydration. One possibility for the origin of anhydrite is direct precipitation from Ca–S-rich fluids, but this requires elevated temperatures (>40 °C) or high salinity. Anhydrite and gypsum have also been formed in laboratory experiments where water is removed from Ca-sulfate aqueous solutions by freezing (Morris et al., 2015). Occurrences of gypsum, bassanite and anhydrite together on Earth are commonly associated with volcanic fumaroles (Jakobsson et al., 2008).

6. Alteration halos in Murray mudstones

The detailed chemical and mineralogical comparisons of the Greenhorn and Lubango drill samples with the Big Sky and Okoruso parent material explore alteration in the Stimson sandstone. Some fractures and associated light-toned halos appear to cross the unconformable boundary between the Murray mudstone and the Stimson sandstone (Watkins et al., submitted for publication). An alteration halo in the underlying Murray mudstone (Figs. 1h, 3) was investigated with ChemCam and APXS, but drill samples were not acquired for mineralogical analyses. The chemical composition outside the lighter-toned alteration zone shows the characteristic chemical signatures of the Murray formation (e.g., elevated Ge and K). Comparisons to APXS data collected from inside the halo show the same pattern of chemical gains and losses as described above for halos in Stimson sandstone (Fig. 9): The lighter-toned, altered sample had higher concentrations of Si, S and P and lower amounts of Mg, Al, Mn, Fe, Ni and Zn. The consistency of the chemical differences between the parent and altered zones in Murray and Stimson rocks indicates that these silica-enriched halos formed from similar solutions and geologic settings.

7. Formation scenario

The fracture-associated halos post-date the deposition and lithification of both the Murray mudstone and the overlying Stimson sandstone and represent the youngest aqueous events explored thus far by the *Curiosity* rover in Gale crater. Multiple fluid stages are responsible for these alteration features, and our model/scenario proceeded as follows: First, fractures occurred in the cemented sediments as a result of burial and compaction (Watkins et al., 2017) or nearby impacts. These fractures now seen at the center of the alteration halos served as conduits for subsurface, acidic fluids or vapors which extensively altered the preexisting mineralogy along the narrow zones (tens of centimeters wide) surrounding the fracture and leached Mg, Al, Mn, Fe, Ni, Zn and other elements. During this first stage of alteration, silicate minerals (pyroxenes and feldspars) were dissolved, resulting in a silica-rich,

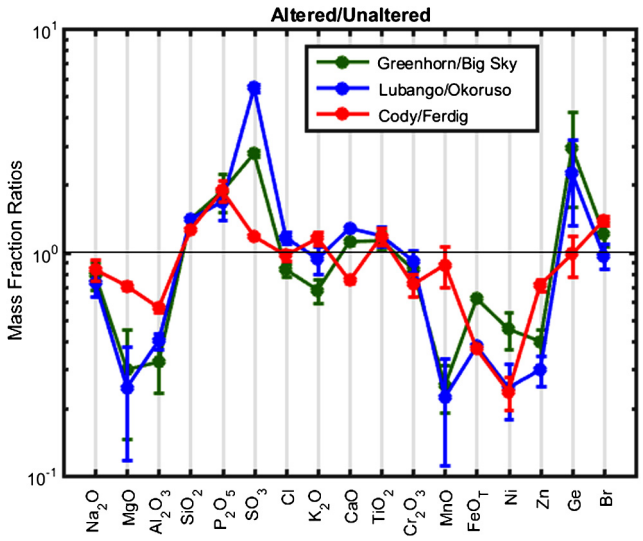

Fig. 9. Chemical ratios of samples within to samples outside alteration halos. Alteration trends within the Murray formation (Cody/Ferdig) are similar to those in Stimson targets and generally exhibit higher Si, P and S and lower Mg, Al, Mn, Fe, Ni and Zn.

X-ray amorphous residue. Second, limited mobility of the leachate, likely due to a low water to rock ratio, resulted in the precipitation of the calcium sulfates within and surrounding the leached rocks. Finally, an evolution of the fluids to neutral/alkaline conditions allowed the introduction of additional silica, carbonates, and possibly phosphates. A single fluid episode with multiple stages is consistent with the observations, though distinct fluid episodes separated in time is also possible.

The acidity of the initial fluid stage, enhancement of the Ge concentrations, and the abundant sulfur (13–15 wt%) in the alteration halos are, together, consistent with fluid interactions with subsurface sulfide reservoirs (Clark and Baird, 1979). Ge appears to be decoupled from Si in the altered fractures (Berger et al., submitted for publication) suggesting a non-silicate origin. Ge may have been captured as fluids propagated through sulfide minerals, which are typically enriched in Ge (Butterman and Jorgenson, 2005). A portion of the sulfur may also have originated from a “dirty sulfate layer” (Schwenzer et al., 2016) remobilized by later stage fluids moving through the basin along the compaction-related pressure gradient. This latter scenario for the origin of the sulfur is consistent with the isotope data from SAM indicating a significant enrichment of $\delta^{34}S$ in the gases evolved from the Greenhorn sample attributed to past atmospheric processing and fractionation of sulfur (Franz et al., in preparation).

8. Conclusions

The *Curiosity* Mars rover in Gale crater conducted a detailed study of fracture-associated halos that cross-cut the Murray mudstone and the overlying Stimson formation sandstone. These alteration halos post-date the deposition and lithification of both the mudstone and the sandstone units and represent the youngest of the major aqueous alteration features studied thus far by the *Curiosity* rover. The primary conclusions are as follows:

– The nature of the chemical and mineralogical changes in the fracture-associated halos relative to the parent sandstone require multiple aqueous alteration stages with fluid chemistries encompassing a wide range of pH. The observations are most consistent with a single aqueous episode with evolving fluid characteristics, but distinct events separated in time may also be possible.

- The initial stage of alteration included extensive acidic leaching with substantial dissolution of mineral phases and removal of metal cations (Mg, Al, Mn, Fe, Ni, Zn and others) resulting in passive enrichment of silica. Amorphous iron sulfates formed during this stage.
- The occurrences of calcium sulfate veins in the Stimson sandstone are nearly uniquely associated with alteration halos and likely represent initial precipitates following the acidic leaching stage. The intimate relationship between the calcium sulfate and the alteration halos suggests limited mobility of the leachate and a low water-to-rock ratio.
- The latter stages of the alteration involved the neutralization of the acidic fluids and the introduction of additional silica, carbonates, and possibly phosphates.

Acknowledgements

We thank the dedicated team of engineers and scientists that makes the *Curiosity* mission possible. This research was supported by the NASA Mars Science Laboratory Mission. A portion of this work was carried out at the Jet Propulsion Laboratory, California Institute of Technology under a contract with the National Aeronautics and Space Administration. We thank the staff of Malin Space Science Systems for production of the Mastcam and MAHLI image products shown herein. We thank an anonymous reviewer and S. Karunatillake for thoughtful comments.

Appendix A. Supplementary material

Supplementary material related to this article can be found online at http://dx.doi.org/10.1016/j.epsl.2017.04.033.

References

Achilles, C., Downs, R.T., Ming, D.W., et al., submitted for publication. Mineralogy of an active eolian sediment from the Namib Dune, Gale Crater, Mars. J. Geophys. Res.

Anderson, R.C., et al., 2012. Collecting samples in Gale Crater, Mars; an overview of the Mars Science Laboratory sample acquisition, sample processing and handling system. Space Sci. Rev. 170, 57–75. http://dx.doi.org/10.1007/s11214-012-9898-9.

Banham, S.G., Gupta, S., Rubin, D.M., et al., in preparation. Anatomy of an ancient aeolian sandstone on Mars: the Stimson formation, Gale crater, Mars.

Berger, J.A., et al., submitted for publication. Zinc and germanium in the sedimentary rocks of Gale crater on Mars indicate hydrothermal enrichment followed by diagenetic fractionation. J. Geophys. Res.

Bernstein, L.R., 1985. Germanium geochemistry and mineralogy. Geochim. Cosmochim. Acta 49, 2409–2422.

Bish, D.L., et al., 2013. X-ray diffraction results from Mars Science Laboratory: mineralogy of Rocknest at Gale Crater. Science 341. http://dx.doi.org/10.1126/science.1238932.

Blake, D.F., et al., 2012. Characterization and calibration of the CheMin mineralogical instrument on Mars Science Laboratory. Space Sci. Rev. 170, 341–399. http://dx.doi.org/10.1007/s11214-012-9905-1.

Blake, D.F., et al., 2013. Curiosity at Gale Crater, Mars: characterization and analysis of the Rocknest sand shadow. Science 341. http://dx.doi.org/10.1126/science.1239505.

Butterman, W.C., Jorgenson, J.D., 2005. Mineral Commodity Profiles: Germanium. USG Open-File Report 2004-1218.

Calef III, F.J., Parker, T., 2016. MSL Gale Merged Orthophoto Mosaic. NASA Planetary Data System Imaging Node PDS Annex. U.S. Geological Survey. Available from: http://bit.ly/MSL_Basemap.

Chipera, S.J., Bish, D.L., 2013. Fitting full X-ray diffraction patterns for quantitative analysis: a method for readily quantifying crystalline and disordered phases. Adv. Mater. Phys. Chem. 3 (1A), 47–53. Special Issue on X-Ray Diffraction.

Clark, B.C., Baird, A.K., 1979. Is the martian lithosphere sulfur rich? J. Geophys. Res. 84 (B14).

Edgett, K.S., et al., 2012. Curiosity's Mars Hand Lens Imager (MAHLI) investigation. Space Sci. Rev. 170, 259–317. http://dx.doi.org/10.1007/s11214-012-9910-4.

Franz, H.B., McAdam, A.C., Ming, D.W., et al., in preparation. Large sulfur isotope fractionations in martian sediments.

Frydenvang, J., et al., in press. Diagenetic silica enrichment and late-stage groundwater activity in Gale crater, Mars. Geophys. Res. Lett. http://dx.doi.org/10.1002/2017GL073323.

Gellert, R., Clark, B.C., 2015. In-situ compositional measurements of rocks and soils with the Alpha Particle X-ray Spectrometer on NASA's Mars rovers. Elements 11, 39–44. http://dx.doi.org/10.2113/gselements.11.1.39.

Golden, D.C., Ming, D.W., Morris, R.V., Mertzman, S.A., 2005. Laboratory-simulated acid-sulfate weathering of basaltic materials: implications for formation of sulfates at Meridiani Planum and Gusev crater, Mars. J. Geophys. Res., Planets 110. http://dx.doi.org/10.1029/2005JE002451.

Grant, J.A., 2005. Isocon analysis: a brief review of the method and applications. Phys. Chem. Earth 30, 997–1004.

Grotzinger, J.P., et al., 2015. Deposition, exhumation, paleoclimate of an ancient lake deposit, Gale crater, Mars. Science 350. http://dx.doi.org/10.1126/science.aac7575.

Harouiya, N., et al., 2007. The dissolution kinetics and apparent solubility of natural apatite in closed reactors at temperatures from 5 to 50 °C and pH from 1 to 6. Chem. Geol. 244, 554–568.

Hurwitz, S., Lowenstern, J.B., 2014. Dynamics of the Yellowstone hydrothermal system. Rev. Geophys. 51, 375–411. http://dx.doi.org/10.1002/2014RG000452.

Jakobsson, S.P., Leonardsen, E.S., Balic-Zunic, T., Jonsson, S.S., 2008. Encrustations from three recent volcanic eruptions in Iceland: the 1963–1967 Surtsey, the 1973 Edfell and the 1991 Hekla eruptions. Natturufraedistofnunar 52.

Krauskopf, K.B., 1956. Dissolution and precipitation of silica at low temperatures. Geochim. Cosmochim. Acta 10, 1–26. http://dx.doi.org/10.1016/0016-7037(56)90009-6.

Mahaffy, P.R., et al., 2012. The Sample Analysis at Mars investigation and instrument suite. Space Sci. Rev. 170, 401–478.

Malin, M.C., Ravine, M.A., Caplinger, M.A., Ghaemi, F.T., Schaffner, J.A., Maki, J.N., Bell III, J.F., Cameron, J.F., Dietrich, W.E., Edgett, K.S., Edwards, L.J., Garvin, J.B., Hallet, B., Herkenhoff, K.E., Heydari, E., Kah, L.C., Lemmon, M.T., Minitti, M.E., Olson, T.S., Parker, T.J., Rowland, S.K., Schieber, J., Sletten, R., Sullivan, R.J., Sumner, D.Y., Yingst, R.A., Duston, B.M., McNair, Sean, Jensen, Elsa H., submitted for publication. The Mars Science Laboratory (MSL) Mast cameras and Descent imager: I. Investigation and instrument descriptions. Earth Space Sci.

McCollom, T.M., Donaldson, C., 2016. Mobility of phosphorus in acid-sulfate environment on earth and Mars. In: 47th LPSC, #1690.

Ming, D.W., et al., 2008. Geochemical properties of rocks and soils in Gusev Crater, Mars: results from the Alpha Particle X-Ray Spectrometer from Cumberland Ridge to Home Plate. J. Geophys. Res. 113, E12S39. http://dx.doi.org/10.1029/2008JE003195.

Morris, R.V., et al., 2000. Mineralogy, composition, and alteration of Mars Pathfinder rocks and soils: evidence from multispectral, elemental, and magnetic data on terrestrial analogue, SNC meteorite, and Pathfinder samples. J. Geophys. Res., Planets 105, 1757–1817. http://dx.doi.org/10.1029/1999JE001059.

Morris, R.V., Rampe, E.B., Graff, T.G., et al., 2015. Transmission X-ray diffraction (XRD) patterns relevant to the MSL CheMin amorphous component: sulfates and silicates. In: 46th LPSC, 2434.

Morris, R.V., et al., 2016. Silicic volcanism on Mars evidenced by tridymite in high-SiO_2 sedimentary rock at Gale crater. Proc. Natl. Acad. Sci. USA 113, 7071–7076.

Morrison, S.M., Downs, R.T., Blake, D.F., et al., submitted for publication. Crystal chemistry of martian minerals from Bradbury Landing through Naukluft Plateau, Gale Crater, Mars. Am. Mineral.

Nesbitt, H.W., 1979. Mobility and fractionation of rare earth elements during weathering of a granodiorite. Nature 279, 206–210.

Nesbitt, H.W., Young, G.M., 1982. Early Proterozoic climates and plate motions inferred from major element chemistry of lutites. Nature 299, 715–717.

Oelkers, E.H., Schott, J., Devidal, J.L., 1994. The effect of aluminum, pH, and chemical affinity on the rates of aluminosilicate dissolution reactions. Geochim. Cosmochim. Acta 58, 2011–2014. http://dx.doi.org/10.1016/0016-7037(94)90281-X.

Robertson, K., Bish, D., 2013. Constraints on the distribution of $CaSO_4 \cdot nH_2O$ phases on Mars and implications for their contribution to the hydrological cycle. Icarus 223, 407–417.

Ruff, S.W., et al., 2011. Characteristics, distribution, origin, and significance of opaline silica observed by the Spirit rover in Gusev crater, Mars. J. Geophys. Res. 116. http://dx.doi.org/10.1029/2010je003767.

Salmimies, R., Mannila, M., Kallas, J., Hakkien, A., 2011. Acidic dissolution of magnetite: experimental study on the effects of acid concentration and temperature. Clays Clay Miner. 59 (2), 135–146. http://dx.doi.org/10.1346/CCMN.2011.0590203.

Schroeer, D., 1970. The Mössbauer effect in microcrystals. In: Gruberman, I.J. (Ed.), Mössbauer Effect Methodology. Plenum, NY.

Schwenzer, S., et al., 2016. Fluids during diagenesis and sulfate vein formation in sediments at Gale crater, Mars. Meteorit. Planet. Sci. 51 (11).

Shukla, J., Mohandas, V.P., Kumar, A., 2008. Effect of pH on the solubility of $CaSO_4$–$2H_2O$ in aqueous NaCl solutions and physicochemical solution properties at 35 °C. J. Chem. Eng. Data 53, 2797–2800.

Sracek, O., et al., 2004. Geochemical characterization of acid mine drainage from a waste rock pile, Mine Doyon, Quebec, Canada. J. Contam. Hydrol. 69, 45–71.

Stefansson, A., Gislason, S., Arnorsson, S., 2001. Dissolution of primary minerals in natural waters II. Mineral saturation state. Chem. Geol. 172, 251–276.

Sutter, B., et al., submitted for publication. Evolved gas analyses of sedimentary rocks and eolian sediment in Gale Crater, Mars: results of the Curiosity rover's Sample Analysis at Mars (SAM) instrument from Yellowknife Bay to the Namib Dune. J. Geophys. Res.

Thompson, L.M., et al., 2016. Potassium-rich sandstones within the Gale impact crater, Mars: the APXS perspective. J. Geophys. Res. Planets 121, 1981–2003. http://dx.doi.org/10.1002/2016JE005055.

Treiman, A.H., et al., 2016. Mineralogy, provenance, and diagenesis of a potassic basaltic sandstone on Mars: CheMin X-ray diffraction of the Windjana sample (Kimberley area, Gale Crater). J. Geophys. Res., Planets 121, 75–106. http://dx.doi.org/10.1002/2015JE004932.

Vaniman, D.T., et al., 2014. Mineralogy of a mudstone at Yellowknife Bay, Gale Crater, Mars. Science 343. http://dx.doi.org/10.1126/science.1243480.

Vaniman, D.T., et al., 2017. Calcium sulfates at Gale Crater and limitations on gypsum stability. In: 48th LPSC.

Watkins, J., et al., submitted for publication. Geometry and significance of an erosional unconformity on Mars, base of Stimson formation, Gale crater. J. Geophys. Res. Planets.

Watkins, J., Grotzinger, J.P., Avouac, J-P., 2017. Fracture formation by compaction-related burial in Gale crater, Mars: implications for the origin of Aeolis Mons. In: 48th LPSC, #3019.

Wiens, R.C., et al., 2012. The ChemCam instrument suite on the Mars Science Laboratory (MSL) rover: body unit and combined system tests. Space Sci. Rev. 170, 167–227.

Zimbelman, D.R., Rye, R.O., Breit, G.N., 2005. Origin of secondary sulfate minerals on active andesitic stratovolcanoes. Chem. Geol. 215, 37–60.